Nanoscale

Creating ground truth for nanocrystal morphology: A fully automated pipeline for unbiased transmission electron microscopy analysis

Journal:	*Nanoscale*
Manuscript ID	NR-ART-08-2022-004292.R1
Article Type:	Paper
Date Submitted by the Author:	22-Sep-2022
Complete List of Authors:	Williamson, Emily; University of Southern California, Chemistry Ghrist, Aaron; Fritz Haber Institut der Max-Planck-Gesellschaft, Molecular Physics; University of Southern California, Chemistry Karadaghi, Lanja; University of Southern California, Smock, Sara; University of Southern California, Chemistry Barim, Gözde; University of Southern California, Chemistry Brutchey, Richard; University of Southern California, Chemistry

Creating ground truth for nanocrystal morphology: A fully automated pipeline for unbiased transmission electron microscopy analysis

Emily M. Williamson,[a‡] Aaron M. Ghrist,[a‡] Lanja R. Karadaghi,[a] Sara R. Smock,[a] Gözde Barim,[a] and Richard L. Brutchey[a*]

Abstract: Control over colloidal nanocrystal morphology (size, size distribution, and shape) is important for tailoring the functionality of individual nanocrystals and their ensemble behavior. Despite this, traditional methods to quantify nanocrystal morphology are laborious. New developments in automated morphology classification will accelerate these analyses but the assessment of machine learning models is limited by human accuracy for ground truth, causing even unsupervised machine learning models to have inherent bias. Herein, we introduce synthetic image rendering to solve the ground truth problem of nanocrystal morphology classification. By simulating 2D images of nanocrystal shapes *via* a function of high-dimensional parameter space, we trained a convolutional neural network to link unique morphologies to their simulated parameters, defining nanocrystal morphology quantitatively rather than qualitatively. An automated pipeline then processes, quantitatively defines, and classifies nanocrystal morphology from experimental transmission electron microscopy (TEM) images. Using improved computer vision techniques, 42,650 nanocrystals were identified, assessed, and labeled with quantitative parameters, offering a 600-fold improvement in efficiency over best-practice manual measurements. A classification algorithm was trained with a prediction accuracy of 99.5%, which can successfully analyze a range of concave, convex, and irregular nanocrystal shapes. The resulting pipeline was applied to differentiating two syntheses of nominally cuboidal $CsPbBr_3$ nanocrystals and uniquely classifying binary nickel sulfide nanocrystal phase based on morphology. This pipeline provides a simple, efficient, and unbiased method to quantify nanocrystal morphology and represents a practical route to construct large datasets with an absolute ground truth for training unbiased morphology-based machine learning algorithms.

Introduction

Engineered colloidal nanocrystals are of interest because of their unique size- and shape-dependent chemical and physical properties.[1,2] Control over nanocrystal morphology (including nanocrystal size, size distribution, and shape) is critical to tailor and ultimately maximize the functionality of individual nanocrystals and their ensembles.[3–6] That is, it is well established that nanocrystal morphology has a direct impact on a myriad of functional properties, including catalytic behavior, optoelectronic and plasmonic effects, and biological uptake for drug delivery and imaging.[7–11] In the overwhelming majority of cases, the resulting morphologies of colloidally prepared nanocrystals are assessed by transmission electron microscopy (TEM), which produces an image with a 2D projection of the 3D nanocrystal. Despite the significance of nanocrystal morphology, the published best practice for determining nanocrystal size and size distribution, for example, relies on the analysis of very small populations ($N \approx 300$ nanocrystals).[12] This is because despite recent advances in analysis methods, image analysis is most frequently done by hand, which introduces human bias, is slow and laborious, and necessarily results in small population statistics. With advances in instrumentation, it is now possible to acquire increasingly larger volumes of TEM images in shorter periods of time, which further exacerbates these analytical challenges and bottlenecks.

Alternatively, image analysis can be done using public domain image processing programs, such as ImageJ,[13] Ilastik,[14] MIPAR™,[15] 'binary DoG' method,[16] Py-EM and SerialEM.[17] These provide some improvements in terms of scaling up data analysis, but nanocrystal detection is only conclusive for well-defined and -separated nanocrystals. Advancements to account for noisy backgrounds, nanocrystal agglomeration, and lower-quality images have been proposed *via* incorporation of modules from different platforms, as exemplified by groups like Qian et al.,[18] Park et al.,[19] and Cervera et al.[20] However, outputs are limited to ensemble averages of a few geometric descriptors, such as 2D area, and sacrifice irregular and concave morphologies for segmentation accuracy.[20,21] This often leads to arbitrary, nongeometric shape descriptors being reported in the literature, including zoomorphic terms such as "nanourchins" and "nanotadpoles" ,[22,23] because of the qualitative nature of parsing shapes. These challenges complicate the description and quantification of nanocrystal morphology by TEM analysis.[24–27]

The incorporation of image processing platforms with machine learning (ML) algorithms presents a solution to these challenges by opening the door for automated nanocrystal morphology classification in a statistical manner. Such advancements will enable high-throughput morphology assessments and universal reporting to aid the incorporation of literature data into ML datasets.[28] One of the first attempts at automated morphology classification was done by Laramy et al.,[29] who measured the distance from the center of each nanocrystal to its edge as a function of angle, $d(\theta)$. Boselli et al.[11] and Lee et al.[21] expanded on this work by quantitatively classifying morphologies into a predetermined number of shape groups *via* different image processing techniques. Most recently, AutoDetect-mNP by Wang et al. offered an unsupervised algorithm for automated morphology analysis.[30] However, such techniques are still in their infancy.[31–34] Generalizability limitations and human bias remain problematic, with the solution to one usually coming at the cost of the other.[11,16,29,30] Generalizability and highly accurate nanocrystal detection can be achieved *via* complex image processing techniques, but such methods are either incapable of differentiating between the shapes and shape attributes of individual nanocrystals in the sample ensemble for subsequent classification or typically require supervision with human-generated ground truth labels to be incorporated into ML platforms[30,15,17,18,35–39] Unsupervised cluster algorithms, such as AutoDetect-mNP, create shape group classifications based on minimized probability statistics, such as Hu moments, that ostensibly removes bias. This is sometimes coined "soft classification" instead of the predetermined groups characteristic of classification algorithms, but the unsupervised nature of the image processing typically lacks the complexity needed to classify a diverse array of morphologies without multiple manual interventions.[16,30] Either way, there is currently no standardized method of quantitatively analyzing diverse ensembles of nanocrystals to uniquely identify shapes and the distribution of shapes.[28,40]

With this in mind, a barrier in the progression of automated image analysis and classification for colloidal nanocrystals is the absence of an unbiased morphological ground truth when training the ML models.[36] With the ground truth for training and testing remaining in the hands of human experts, even unsupervised models are still inherently limited to human accuracy and rooted in human bias since the evaluation is reliant on the comparison to the *status quo* biased methods. Herein, we create a ground truth for nanocrystal morphology classification by exploiting the unbiased nature of deep learning in conjunction with the analytical assurance of simulation. The general workflow of automated morphology classification has three main components: (1) nanocrystal detection (segmentation), (2) feature extraction, and (3) classification. Recent studies have utilized synthetic image rendering as a ground truth to solve the annotation problem in segmentation of nanocrystal images *via* deep learning, proving to be an important step in removing

the bias in initial nanocrystal detection.[37,41,37] We extend this method to feature extraction, thereby creating a ground truth for morphology classification. By simulating a theoretically infinite number of individual nanocrystal morphologies *via* a quantifiable, parametrically continuous mathematical function, we train a convolutional deep neural network (CNN) to perform the simulation in reverse by predicting the point in parameter space that best corresponds to each pixelated, noisy nanocrystal image. This links experimental morphologies to a unique combination of parameters and thus defines nanocrystal morphology quantitatively rather than qualitatively. We then create an unsupervised, automated pipeline that accurately processes, quantitatively defines, and classifies the morphologies of nanocrystals from experimental TEM images, utilizing the neural network output as ground truth for classification (Scheme 1). The pipeline utilizes computer vision techniques to separate and identify ranges of concave, convex, and agglomerated nanocrystals. To the best of our knowledge, this is the first example of a non-human ground truth in nanocrystal morphology classification, and therefore the first example of a pipeline that is designed to eliminate human bias. The pipeline demonstrates accuracy across a wide range of nanocrystal morphologies and efficiently creates a viable dataset large enough to train subsequent ML models to near perfect accuracy. This pipeline can be easily implemented by any researcher, with a simple 5-step guide included in the MATLAB code on Github for those with little-to-no coding background.

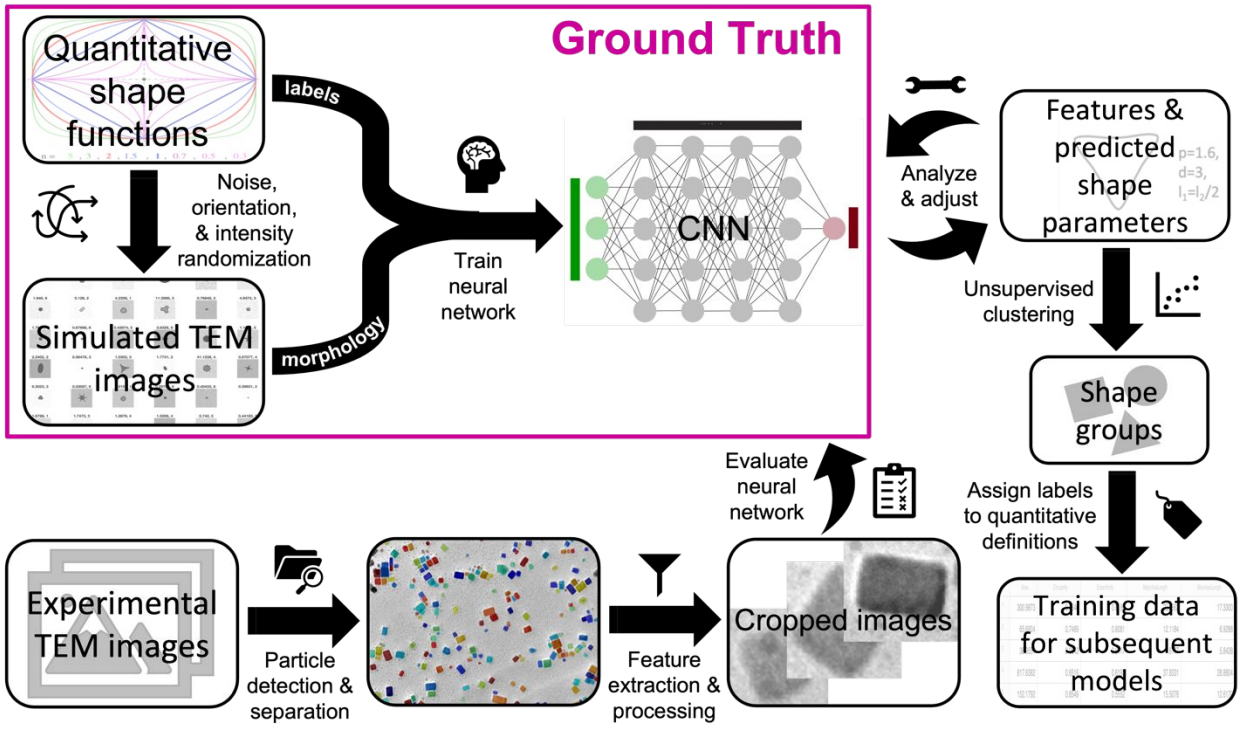

Scheme 1 Visualization of full pipeline for TEM image analysis.

Results and discussion

Machine learning pipeline

The components for our algorithm include a neural network trained on simulated images of individual nanocrystals to create a morphological ground truth, which is used to evaluate the output of a parallel image processing algorithm that detects, separates, crops, and extracts the morphological features of nanocrystals in experimental TEM images. The trained neural network predicts and assigns three shape parameter values for each detected experimental nanocrystal that, cohesively, best define the overall morphology in 2D virtual space according to the simulation function. These shape parameters are then utilized to cluster the nanocrystals into shape groups in an unsupervised manner, and act as ground truth labels to train morphology classification algorithms (Scheme 1).

Image processing. The first step in automated morphology classification is image processing. Efficient and accurate segmentation of colloidal nanocrystals in the foreground of an experimental TEM image is essential for accurate nanocrystal detection, feature extraction, cropping, and eventual classification. Furthermore, the quality of the TEM images inputted into a neural network directly affects its accuracy and precision. As a result, segmentation is a widely studied area of image processing, with techniques ranging from simple thresholding to complex neural networks to predict an accurate image segmentation.[37,41–44] We opt for a simple but effective approach to increase the pipeline generalizability (Fig. 1), described in more detail in the ESI†. Processing concave shapes has been an ongoing problem in shape classification as concavity is commonly used as a way to filter out overlapping nanocrystals, which inhibits the analysis of naturally concave morphologies.[19,29,30,35,45] We address this challenge by analyzing the connectivity and intensities of each pixel in a segmented image *via* MATLAB's *watershed* function, which identifies connected components as "water wells" that fill to a certain level before the pixels begin to intersect with neighboring nanocrystals (Fig. 1c). Each "well" therefore indicates an individual nanocrystal center, whose edges are uniformly eroded in the segmentation to remove any overlap with other nanocrystals while maintaining the integrity of the nanocrystal morphology. The eroded nanocrystal mask is subsequently rebuilt in an equal but opposite manner *via* dilation to obtain the correct size and shape before cropping and feature analysis. Once segmentation is complete, 30 different features are calculated for each nanocrystal, as defined in the ESI†. Extremely agglomerated samples where individual nanocrystals cannot be distinguished even qualitatively can be filtered out *via* implementing a threshold for extreme outliers. Although this occasionally filters out "accurate" nanocrystals, it removes the inaccurate segmentations without limiting the shapes that can be accurately processed, and in our experience the loss of the accurate nanocrystal renderings remains insignificant to the overall result. Bounding box and centroid data are then used to visualize the accuracy of the segmentation and crop each TEM image into smaller images of individual nanocrystals (Fig. 1d). Lastly, the cleaned, cropped images are compressed to normalize image size for implementation into the neural network, in accordance with Scheme 1.

In addition to visualizing the bounding boxes for each detected nanocrystal (Fig. 1d), we assessed the ability of the pipeline to handle nanocrystal agglomeration and misclassification. Nanocrystals from a single batch of product were imaged *via* TEM with three different degrees of agglomeration: non-overlapping, semi-overlapping, and almost entirely overlapping (Fig. S1†). Each image was input into the pipeline separately to assess the effects of agglomeration on the output. Across the three levels of agglomeration, each image was similarly classified into seven shape groups with average sizes within a standard deviation of each other. The non-overlapping sample had an average size of 20.0 ± 13.8 nm, the semi-overlapping sample had an average size of 18.0 ± 8.3 nm, and the very agglomerated sample had an average size of 16.1 ± 7.4 nm. The

decreasing size and polydispersity with increasing agglomeration is concurrent with accurate nanocrystal detection, as more agglomeration means a denser population of nanocrystals, so large outliers have less of an influence. If agglomeration was causing a significant effect on detection, one could assume that the size and polydispersity of the detected nanocrystals would get larger due to agglomerated masses being classified as large, singular particles. Tables of the average and standard deviation of shape features across each shape group were also consistent and independent agglomeration (Tables S1-S6†), further supporting that agglomeration is non-significant in detection accuracy for the pipeline.

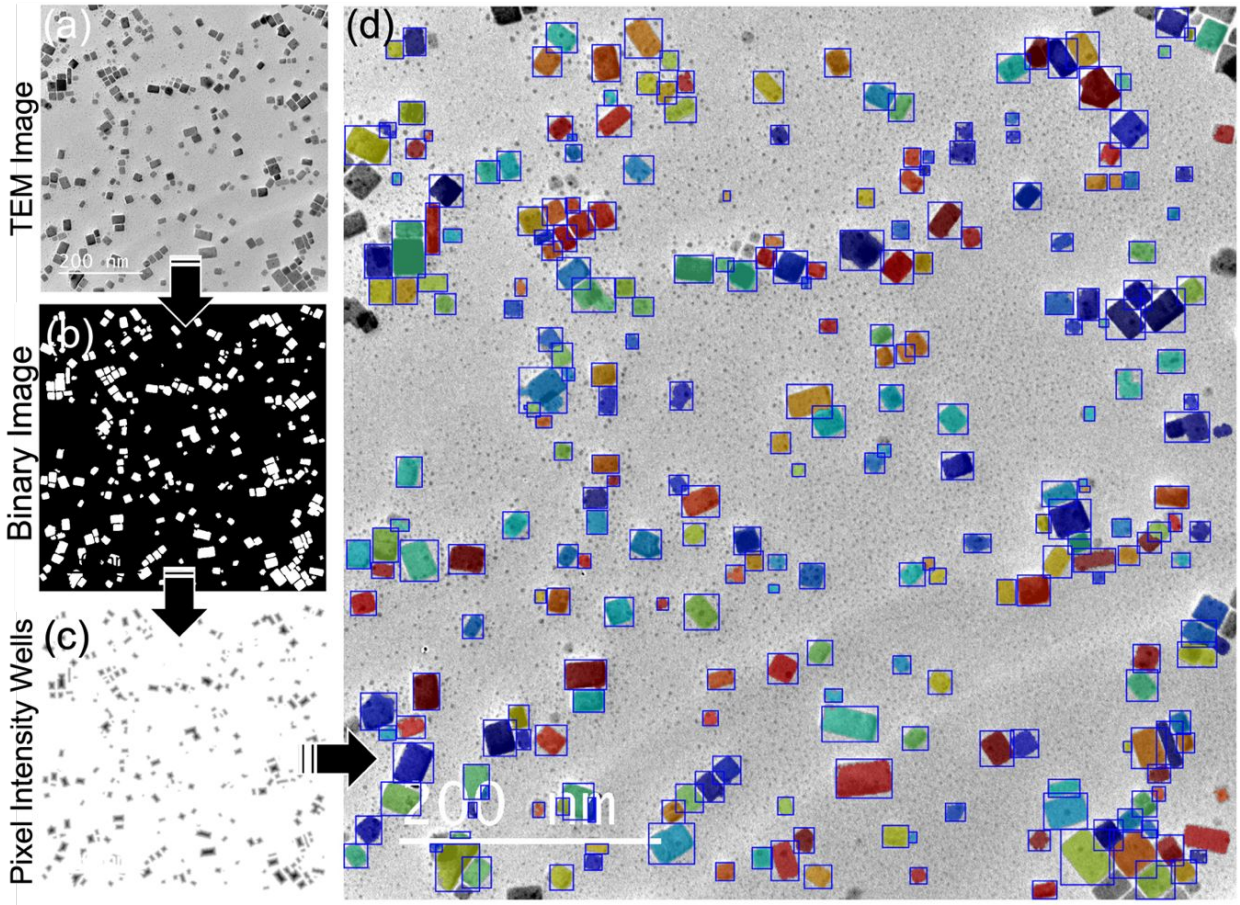

Fig. 1 General workflow of the TEM image preprocessing method. (a) Original bright field TEM image of $CsPbBr_3$ nanocrystals. (b) Binary image segmentation after contrast adjustment, filtering, and processing. (c) "Water wells" of pixel intensities in each connected component to identify and separate agglomerated nanocrystals. (d) Individual nanocrystal segmentations plotted as colors overlaid onto the original TEM image, with their respective bounding boxes used for cropping and implementation into the neural network. Nanocrystals connected to the edges and joined with the scale bar are removed.

Creating morphological ground truth. Simulated images of individual nanocrystals were used as ground truth in the training of a convolutional neural network to directly map a unique morphology to a quantitative description. Images were generated from a polar function (and the corresponding pre-defined parameter space) that defines a large class of closed curves with differing degrees of radial symmetry (Fig. 2a and ESI†). This extension of the class of 'super-

ellipses' provides a natural way of continuously parameterizing the curvature of the closed curves, yet is the first time it has been applied to nanocrystal morphologies.[46] When simulating ground truth to train the neural network, parameter values were randomly drawn from the distributions given in Table S7†. These values were used to plot nanocrystal morphologies in polar space (radius R as a function of $\theta \in [0,2\pi]$) and physically correspond to curvature (p-norm, or p), the number of major axes (d), the ratio between the major and minor axis lengths (L_{ratio}), and a random rotational phase shift (ϕ) (eq 1). The ground truth therefore consists of each simulated image stored in a data matrix and a labels matrix with each image's corresponding parameter array that was used to generate the curve. Random sampling helps avoid training the network to 'recognize' specific parameter values when the experimental images can have any parameter value. Introducing a random distribution of rotational phase shifts, intensity contrasts, pixelation, and Poisson background noise account for the non-ideal conditions of experimental TEM images. Fig. 2b demonstrates the generalizability of this model through the generation of morphologies that are common to colloidal nanocrystals (*i.e.*, qualitative morphology labels such as circles, rectangles, kites, and urchins), along with abnormal and asymmetric morphologies (Fig. S3†).

$$R = \left[\left(L_{ratio}\left|\cos\left(\frac{d}{2}(\theta+\phi)\right)\right|\right)^{p} + \left|\sin\left(\frac{d}{2}(\theta+\phi)\right)\right|^{p}\right]^{-1/p} \quad (1)$$

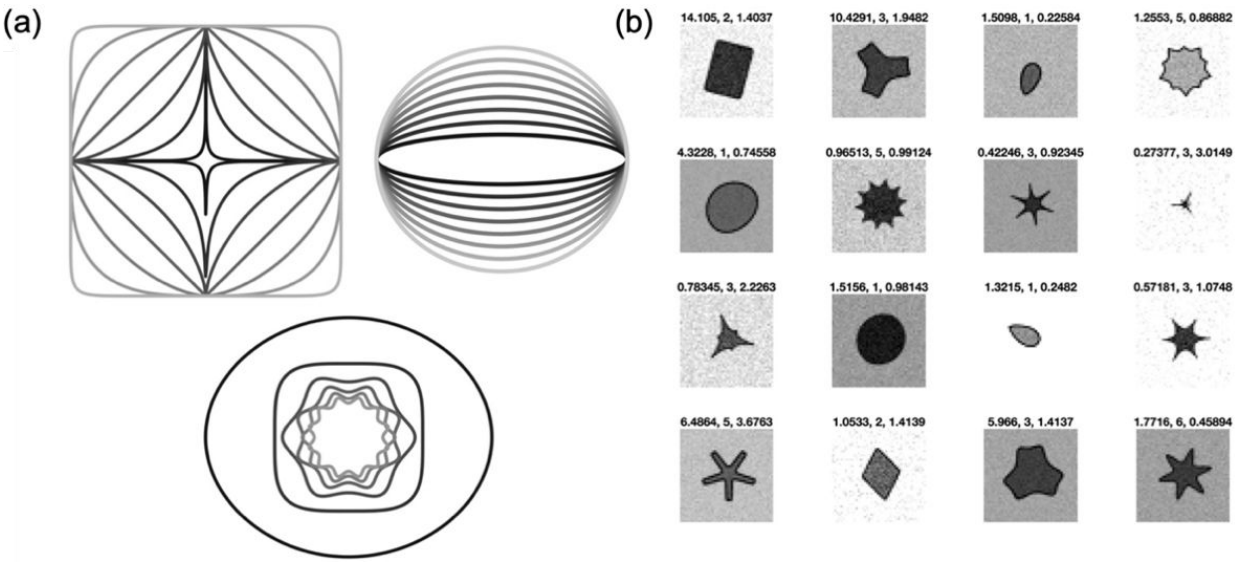

Fig. 2 Overview of outputs from model to generate simulated nanocrystal morphologies to create a ground truth. (a) Demonstration of how varying individual parameters in the model while keeping the others constant affects the generated nanocrystal shape: Upper left, p-norm; upper right, L_{ratio}; bottom, number of major axes d (size adjusted for clarity). (b) Sampling of simulated nanocrystal TEM images. The labels for each image are (p, d, L_{ratio}).

From this model, 65,000 simulated TEM images depicting distinct nanocrystal morphologies and their corresponding ground truth parameter values (p, d, and L_{ratio}) were generated and used to train a convolutional neural network (CNN) in a 70/10/20 train/validate/test split. This network optimally finds the underlying parameters of nanocrystal shape *via* regression from an input TEM image. Choices regarding the model design are detailed in ESI†. To evaluate the trained CNN, the validation set was drawn independently from the total set of simulated

images, and the validation root mean squared error (RMSE) was calculated to indicate the performance of the network over the whole dataset. Regression neural networks minimize the distance between the ground truth point and the evaluated point in parameter space, so it is impossible to optimize the network on classification accuracy, but they have the advantage of outputting quantitative estimates for the parameters, which is requisite for any eventual optimization of morphology. Furthermore, we used a learning curve (Fig. 3a) to compare the training RMSE to the validation RMSE as a function of training data used. This shows the estimation error was optimally minimized without reaching the region of overfitting, as validation error nearly identically follows the sample error as it approaches the limit of the approximation error. The total decrease in RMSE with iteration indicates that the adjusted network parameters are increasing the accuracy of the predicted model parameters. The validation RMSE leveling off but not increasing as the training RMSE decreases indicates that a reasonable learning rate was chosen, and the network is well-trained.[47] Additional standard methods were used to assess the quality of the network training. The quantile-quantile (Q-Q) plot shown in Fig. 3b illustrates a deviation between ground truth (imposed) number of dimensions and the predicted number of dimensions at a high number of primary axes, indicating that the model slightly overpredicts for $d = 1$ and underpredicts for $d = 5, 6$ (*i.e.*, the network loses its ability to distinguish between images generated with increasingly large radial symmetry). This is a sensible interpretation, as even human visual perception struggles to distinguish between shapes with high degrees of 2D symmetry even without considering the additional pixelation and noise. This plot also demonstrates that while the ground truth dimension is discrete, the network prediction is continuous, as discretization would introduce a potential systematic bias. The RMSE plot against the ground truth parameters in Fig. 3c shows the model is extremely good for small p, where the morphology changes the most with small changes in p, and large curvature p comprises most of the error, indicating that as p increases, there is a small effect on the generated morphologies. Detailed analyses of the chosen evaluation tools are discussed in the ESI†.

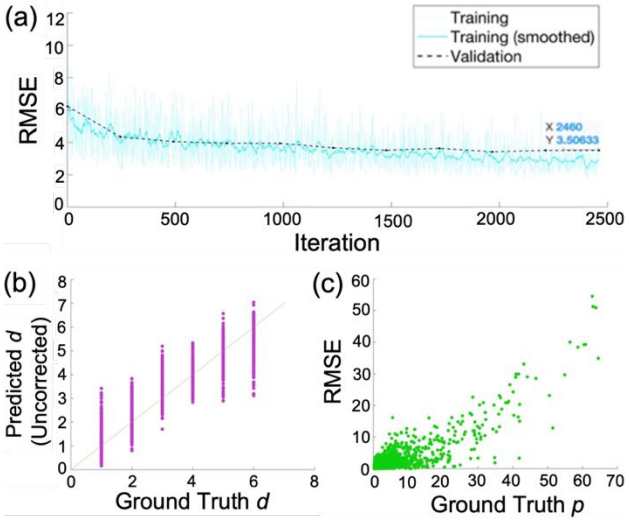

Fig. 3 Diagnostic tools for assessing the quality of the neural network training. (a) Learning curve plotting the root mean square error (RMSE) for individual nanocrystal images as a function of the number of images on which the neural network was trained. (b) Q-Q plot for the number of major axes (d). (c) RMSE-parameter plot for the curvature (p).

After optimizing the network type, number of layers, and network hyper-parameters *via* the evaluation tools, the trained CNN was used to evaluate experimental TEM images pre-processed as described above. The CNN predicts a point in the parameter space comprised of the three ground truth parameters (p, d, L_{ratio}) that best corresponds to the morphology depicted in each cropped image. Using these predicted parameters to 're-simulate' the experimental morphologies enabled a quantitative comparison to the ground truth *via* calculating the *jaccard* similarity coefficient, which averaged around 0.8 out of 1.0 (ESI†).[41] Re-simulation qualitatively illustrates that the predicted parameters are accurate renderings of the experimental nanocrystals (Fig. S33†). While individual ground truth simulations may deviate from their experimental counterparts, the network still performs well over the distribution of the entire testing set, as the training and evaluation of a neural network is a statistical process.

Unsupervised clustering and classification into shape groups. The ground truth predictions for each nanocrystal were concatenated to the 30 morphology features that were extracted in the image processing. In addition to information about the distribution of the nanocrystal parameters, morphology feature data was used to obtain spatial information and pixel scaling data. This aids in removing incorrect segmentations (*i.e.,* near the scale bar) and leads to a more accurate statistical clustering of the nanocrystals into shape groups based on both size and shape. Some features such as FilledImage were used for visualizations of the output. Clustering was unsupervised to further remove human input in the pipeline, which was achieved by calculating the silhouette value to automatically assess cluster quality of K number of clusters within each cluster algorithm, and the cophenet correlation coefficient (*ccc*) to compare alternative cluster solutions obtained using different algorithms. The latter assesses how well the clusterings obtained by each algorithm represent the data in a dendogram tree, scoring each between 0 and 1 (where 1 is the highest quality solution, see ESI†).[48] This approach is simpler than others commonly used in literature but equally effective, thus enhancing speed without losing accuracy.[30,39]

The unsupervised clustering method was optimized by testing three different clustering methods (*i.e.*, K-means, Gaussian mixture model (GMM), and hierarchal linkage tree clustering) with three versions of the output dataset: (1) solely morphological features (2) solely the three shape parameters outputted from the CNN, and (3) both (1) and (2) (ESI†). The results of the clustering algorithm optimization are summarized in Tables S8† and S9†. K-means clustering outperformed the other two methods with every dataset, and the dataset of combined morphology features and CNN output parameters outperformed all other datasets across all clustering methods. Additionally, the combination of optimal method (K-means) and optimal dataset (3) resulted in the highest overall *ccc* of 0.9483. Consequently, we used K-means clustering with a dataset consisting of both the CNN parameters and common morphology descriptors for the unsupervised clustering in the pipeline (all clustering methods took less than a minute, so time was not factored into the decision).

In comparison to the optimal dataset, clustering results from the dataset of only the CNN parameters consistently ranked a close second, whereas the morphology features dataset (*i.e.,* only physical descriptors) consistently performed the worst, by a significant margin (Table S8†). A repetition of the optimization with a dataset from lower quality images followed the same patterns across all combinations, further corroborating this trend (Table S9†). Adhering to the concept that descriptor properties relevant to clustering will improve the predictive power of the model,[49] this result demonstrates that the CNN parameters are significantly more effective in quantitatively defining nanocrystal morphology than common features extracted from image processing. Thus,

they offer a low-dimensional (3D parameter space) and more effective continuous option for describing morphology in experimental design space mapping, where discrete responses cause exponential increases in model complexity. Furthermore, although the addition of the physical features is important for drawing conclusions that are chemically meaningful, they only slightly increase the *ccc* value (*i.e.*, the quality of the clustering), suggesting that the CNN parameters are essential for results that are acceptable to act as ground truth labels. As a result, the final step of the full pipeline was to use this labeled data for automatic training of a classification algorithm, creating a built-in practical use of the output data for researchers. We optimized the classification model *via* Bayesian optimization, which indicated the implementation of a multiclass support vector machine (SVM) model (ESI†).

Experimental applications

Training classification algorithms. Classification models can be vital tools for elucidating high-level connections between experimental parameters and product morphologies and morphology-dependent properties, but their practicality directly correlates to their accuracy.[11,34] To illustrate the effectiveness of the concepts used in the pipeline to create a ground truth for nanocrystal morphology, we investigated different classification models trained using various labeled datasets. The first study utilized large (163 TEM images, N = 42,650 nanocrystals) and small (52 TEM images, N = 13,115 nanocrystals) datasets, which include the three CNN parameters, the unsupervised clustering results, and 10 of the most common morphology features used in similar studies (ESI†). The low-dimensional nature of the morphology feature descriptors and the unsupervised clustering results aid in bridging the gap between the complex morphology information embodied *via* the high-dimensional CNN parameters and their real-world implications about morphology. While the CNN parameters offer a description of morphology that is highly accurate, such a bridge is essential to connect the relationship between that accurate description and the experimental parameters that produced it for further applications. Both datasets consisted of several binary and ternary nanocrystal phases spanning a wide range of morphologies to ensure representation of complex populations notably absent in the literature.[11,21,29,30,41] The performances of the trained models were evaluated by computing the prediction accuracy of the test datasets, or the percentage of correctly classified nanocrystals into shape groups (based on a 2D rendering), from an 80/20 train/test split with 10-fold cross validation. The accuracy of the model trained using the large dataset was 99.5%, misclassifying only 42 out of 8,530 nanocrystals from the test dataset (Fig. S14a†). Training a similar model on the smaller dataset (~30% of the large dataset) did not significantly affect the model accuracy (99.1%), with only 25 out of the 2,623 nanocrystals in the testing set being misclassified (Fig. S14b†). This emphasizes that the pipeline is robust for studies where the number of TEM images is more limited.

When the three CNN parameters were removed and the models were trained using only clustering results predicted from the 10 morphology features as labels, model accuracy of the large dataset was significantly lower at 74.7%, misclassifying 2,155 of the 8,530 nanocrystals in the testing set (Fig. S15a†). Model accuracy of the smaller dataset was even worse, with a test accuracy of 55.7%, misclassifying 1,162 of the 2,623 nanocrystals in the testing set (Fig. S15c†). This demonstrates that the addition of the CNN parameters drastically increases both model training efficiency and accuracy, further supporting their importance in accurate morphology classification. To ensure that the superiority of the models trained using the CNN parameters was not solely due to the addition of three additional variables, three of the 10 morphology features were randomly

removed from the large and small datasets, and the classification algorithm was re-trained with 10 variables: seven morphology features and the three CNN parameters. Model accuracy remained significantly higher than without the inclusion of the CNN parameters, with a test accuracy of 99.2% for the larger dataset and 99.0% for the smaller dataset (Fig. S16†). To further corroborate this result, the classification algorithm was retrained using the large dataset, but this time only including the CNN parameters and four morphology-feature predictors (Fig. S16b†). The test accuracy remained exceptionally high at 98.5%, which was within a standard deviation of the others. This illustrates that implementation of a simulated ground truth *via* deep learning results in nearly perfect classification models for classifying nanocrystal morphology, while simultaneously highlighting the ineffectiveness of a features-only approach.

Morphological differentiation of $CsPbBr_3$ nanocrystals from different syntheses. With the optimal route for morphology classification determined, the full pipeline was implemented to compare two different synthetic methods for the preparation of colloidal $CsPbBr_3$ nanocrystals that are nominally reported to give cuboidal morphologies; that is, the hot-injection and ligand assisted reprecipitation (LARP) methods.[50,51] While 0-D $CsPbBr_3$ nanocrystals are commonly described as cuboids (and 2D projections of the cuboids in TEM images appear as squircles, quantitatively super-ellipses with *p*-norms roughly between 5 and 20), recent studies on the superball form factor of cuboidal edge roundness suggest that a more precise quantification is necessary for accurate differentiation between nanocrystal shape, as such differences may have consequences in terms of nanocrystal optoelectronic properties and/or reactivity (*e.g.*, ion exchange).[52] Here, 7,082 distinct nanocrystals synthesized *via* the hot-injection method (without experimental size selection) were detected from 20 inputted TEM micrographs and analyzed. As determined by the unsupervised cluster evaluation algorithm, the nanocrystals were subsequently classified into four shape groups: small cuboids (group 1), large irregular nanocrystals (group 2), larger cuboids (group 3), and small platelets (group 4) (Fig. 4). The general trends in feature values for each group and their location within the 3D parameter space are illustrated in Fig. S17†. The average and standard deviation of the characteristics of each group were calculated (Tables S10† and S11†) and visualized *via* histograms of the observations for each predictor variable (Fig. 4c-d and Fig. S19†). Each shape group in the histograms are plotted in a different color, enabling the calculation of the normal distribution that corresponds to each group. Analysis of these output results along with the population sizes of each group (Fig. S18†) indicated that ~70% of the ensemble consisted of small cuboids (group 1) with an average 2D area of 62 nm^2 and a high circularity of 0.92 (*i.e.,* more rounded edges), and larger cuboids (group 3) with an average 2D area of 125 nm^2 and sharper corners (circularity = 0.87). About 20% of the ensemble consisted of the more plate-like nanocrystals (group 4) with a significantly higher aspect ratio of 1.8 (as compared to the average aspect ratio of the cuboids falling around 1.2). The remaining 10% of the ensemble was comprised of much larger nanocrystals with irregular morphologies (group 2). This suggests a relatively monodisperse population, which is further supported by the fact that the two cuboidal groups (1 and 3) that describe most of the population are rather monodisperse themselves. Calculation of the size distributions yielded $\sigma/\overline{d} = 20\%$ and 14% for groups 1 and 3, respectively, compared to $\sigma/\overline{d} = 33\%$ for the entire population (Table 1). Furthermore, using these data to train a classification model resulted in an accuracy of 99.6%, only misclassifying six nanocrystals (Fig. S20†), suggesting acceptable ground truth simulations (validated in Fig. S33†).

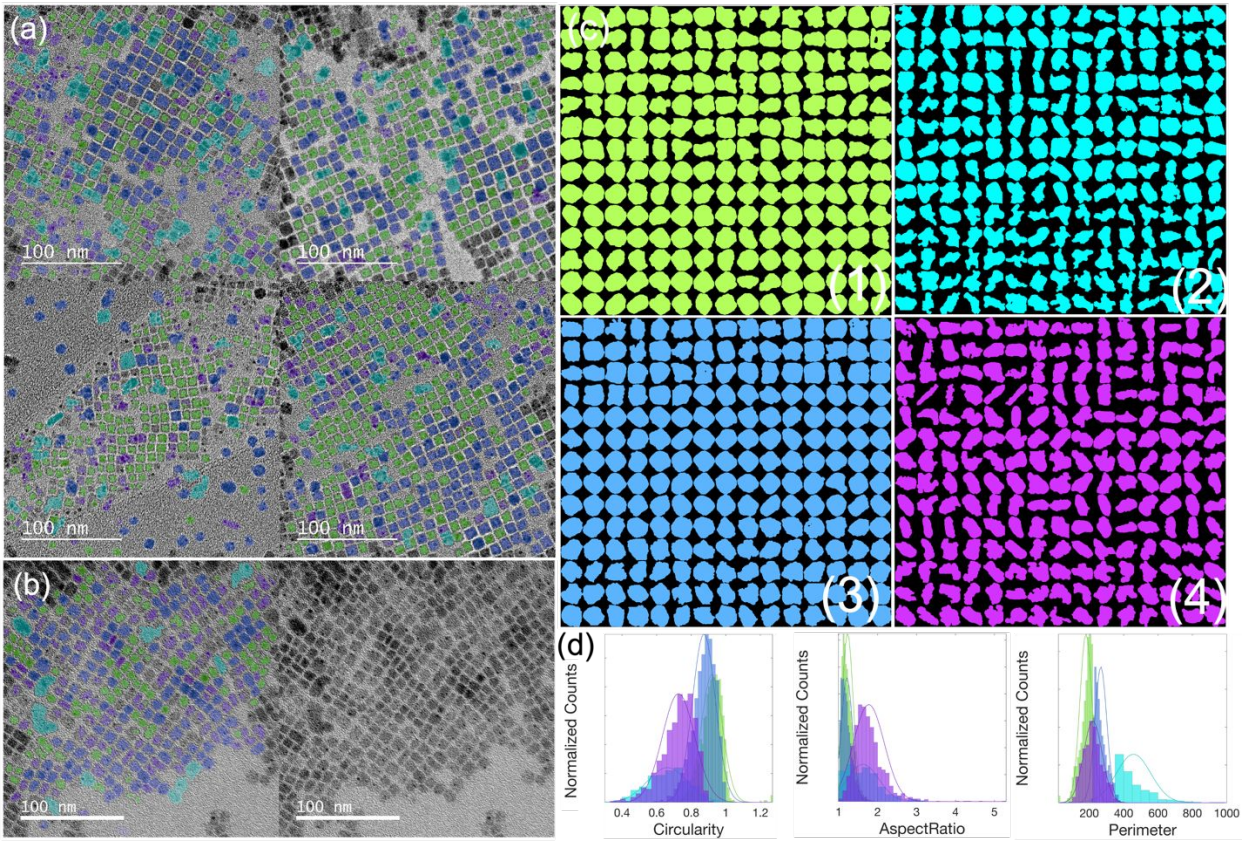

Fig. 4 (a) Classification of the $CsPbBr_3$ nanocrystals resulting from the hot-injection synthesis differentiated by color and overlaid onto original TEM images. Nanocrystals connected to edges are removed. (b) Overlaid shape groupings (left) compared to the original bright field TEM image (right). (c) A subset of 210 nanocrystals from each of the four shape groups. (d) Three exemplary histograms and corresponding normal distributions of feature descriptors (clusters are color coded).

The 20 TEM images were comprised of two different synthetic batches of $CsPbBr_3$ nanocrystals, identically prepared, and thus were analyzed separately to gain insight on synthetic reproducibility of the hot-injection method. Both nanocrystal populations (N = 4,064 and 3,018) were equally clustered into four shape groups with morphologies qualitatively like those described above (Fig. S21-S23† and Fig. S25-S27†, respectively). Statistical analysis of each shape group indicated comparable morphology statistics to each other and to the total product (Table 1 and Tables S10-S15†). Furthermore, the average sizes (defined as the average major axis length) of the total populations were also nearly equivalent (batch 1 = 12.5 nm, batch 2 = 12.1 nm, and total = 12.4 nm). Both batches also followed the same trends in terms of the relative population fractions of nanocrystals belonging to each group. Most nanocrystals belonged to the monodisperse cuboids of groups 1 and 3 (although batch 2 had slightly more of the sharper cornered cuboids), followed by the more oblong platelets of group 4. Each batch had a relatively small population of the larger irregular shapes of group 2 (Fig. S22† and S26†). These data indicate good morphological reproducibility for the hot-injection synthesis of $CsPbBr_3$ nanocrystals and provide a proof of concept for the pipeline to quantify synthetic reproducibility in general.

Table 1 Batch-to-batch morphological comparison of $CsPbBr_3$ nanocrystals synthesized by the hot-injection method.

	Batch 1				***Batch 2***				***Total***			
Shape group	1	2	3	4	1	2	3	4	1	2	3	4
Average size[a] *(nm)*	10.7	26.1	15.6	12.1	8.7	23.8	12.7	12.6	9.7	24.2	13.9	12.8
Size distribution ($\sigma/\bar{d}$)	0.17	0.18	0.14	0.27	0.21	0.18	0.14	0.25	0.20	0.19	0.14	0.27
Total average size (nm)	12.5 ± 3.7				12.1 ± 4.6				12.4 ± 4.1			
Total size distribution ($\sigma/\bar{d}$)	0.30				0.38				0.33			

[a] Average major axis length across all shape groups.

Similarly, 6,427 distinct nanocrystals were detected from 31 TEM micrographs depicting populations that were synthesized by the LARP method, to compare the products to those produced *via* hot injection. This dataset was clustered into six shape groups, whose general shapes are illustrated in Fig. 5c, although relative sizes between the groups (defined in Table 1) are not to scale. Shape groups 1-6 had average sizes of 8.9, 32.2, 15.4, 6.7, 13.1, and 21.9 nm, respectively. Similarly, each had varied size distributions ($\sigma/\bar{d}$), or polydispersities, of 24%, 15%, 15%, 25%, 28% and 30%, respectively. More detailed characteristics of each group were calculated, visualized, and analyzed in an identical manner to that of the hot-injection synthesis (Fig. S29-S31† and Tables S16† and S17†). Analysis of the results indicated that each group had approximately equal representation in the ensemble (~20%), apart from the very large irregular quasi-cuboids of group 2 that made up < 5% of the ensemble (Fig. S30†). This, along with the wide range of average sizes across the groups, suggests a more polydisperse product, which aligns with the polydispersity calculated for the total dataset of 50% (Table 2). The LARP dataset was used to train a classification algorithm, resulting in a test accuracy of 99.3% (Fig. S32†), which corroborated the simulated ground truth for further applications (Fig. S33†).

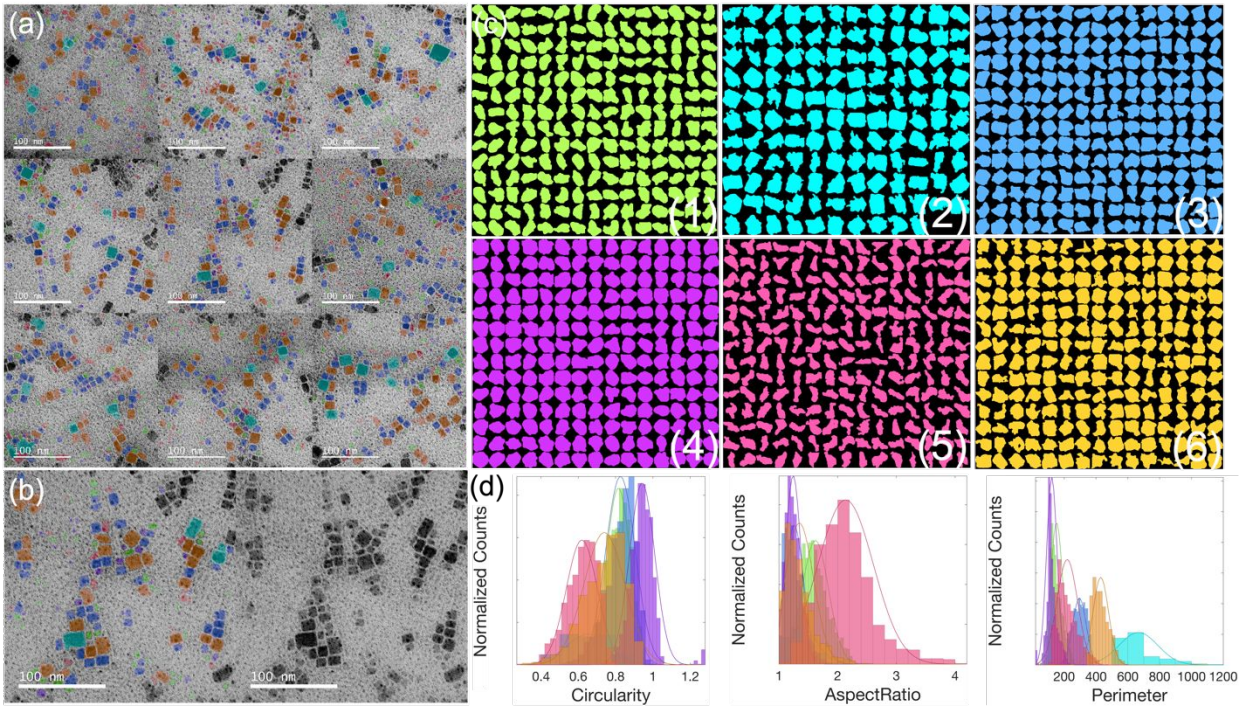

Fig. 5 (a) Classification of the $CsPbBr_3$ nanocrystals resulting from the LARP synthesis differentiated by color and overlaid onto original bright field TEM images. Nanocrystals connected to edges have been removed. (b) Overlaid shape groupings (left) compared to the original TEM image (right). (c) A subset of $\leq$ 210 nanocrystals from each of the six shape groups (d) Three exemplary histograms and corresponding normal distributions of feature descriptors (clusters are color coded).

Comparing the two synthetic methods, LARP yielded significant $CsPbBr_3$ morphological differences from hot injection. The nanocrystals produced *via* hot injection were more well-defined, exemplified both quantitatively by a higher classification accuracy and qualitatively by the nanocrystal segmentations in Fig. 4c and 5c. The average morphologies of each group within the parameter space defined by the CNN parameters in Fig. S33† show that the hot-injection synthesis generally produced more uniform cube-like nanocrystals across the ensemble, whereas the nanocrystal morphologies resulting from the LARP synthesis are more irregular and varied. Additionally, the hot-injection synthesis gave averages sizes ranging from 9.7-24.2 nm across the groups (Fig. S33a†), nearly half of the 6.7-32.2 nm size range seen for the LARP synthesis (Fig. S33b†), suggesting greater monodispersity. This is affirmed by the nanocrystals resulting from the hot-injection synthesis being classified into fewer shape groups (4 vs. 6), as fewer well-defined normal distributions in the predictor variable histograms indicate more morphologically similar populations (*i.e.,* fewer statistically different morphologies) (Fig. S19† and S31† and Tables S10†, S11†, S16†, and S17†). The previously mentioned polydispersities calculated for the entire ensembles only strengthen this claim (33% for hot injection *vs.* 50% for LARP). Qualitatively this makes sense, as the $CsPbBr_3$ nanocrystals resulting from the hot-injection syntheses generally self-assemble upon drop casting onto the TEM grid.[53] Furthermore, a deeper analysis of the groups that characterize the upper bounds of the resultant morphologies (*i.e.,* the outlier groups – group 2 for both syntheses) revealed that group 2 from the LARP synthesis had an average 2D area that was well over two standard deviations greater than that of the hot-injection synthesis (573.7 nm^2 *vs.*

276.4 nm^2, respectively), indicating a drastic difference between the morphological parameter spaces of the two products (Table S10†, S11†, S16†, and S17†). Although it is generally accepted in the literature that the hot-injection method offers a superior morphological product due to more controlled instantaneous nucleation,[53] the pipeline output provides the statistically significant data to support that assertion, and quantifies the morphological differences. Using the CNN to define shape across an entire nanocrystal population therefore helps establish more accurate quantifiable metrics for typically qualitative conclusions about the general trends in nanocrystal syntheses.

Notably, the histograms of all three CNN predictor variables for nanocrystals from both synthetic methods consist of nearly perfectly overlapping normal distributions for each group, whereas the feature descriptors show histograms with much more statistically different distributions for each cluster (Fig. S19† and S31†). This is counterintuitive for clustering data, as separated normal distributions for a specific feature generally indicate a unique cluster, but the data from a single feature is just one dimension of a complex, high-dimensional definition of morphology. If one were to combine the data from several feature histograms into a single histogram, the separated distributions will start to fade if you consider, for example, that a morphology cluster with a high value of circularity would have a low value of a feature like eccentricity. After enough features are combined, the separation between clusters would not exist at all on such a histogram plot. Such is the nature of the CNN parameters. The overlapping distributions on a histogram support the concept of the CNN parameter combination as a high-dimensional quantitative definition of shape for each nanocrystal, which encompasses morphology information equivalent to an entire array of morphology features. While they are poor tools for extracting specific characteristics, they hold a complete picture of high-dimensional data in a low-dimensional form (much like what multidimensional scaling or principal component analysis do for high-dimensional data visualization). This reaffirms their ability to be used as ground truth labels in subsequent training.

The average nanocrystal sizes for both syntheses were also measured by hand by two experienced researchers for comparison. Due to the average size and size distributions of each nanocrystal ensemble being automatically output by the pipeline, thousands of nanocrystals are accurately measured in just minutes. In contrast, the common practice of manually measuring the major axis of $N \geq 300$ nanocrystals per sample not only takes considerably longer but is subject to inaccurate population sampling due to human bias and error.[12,13] For the hot-injection method, the average nanocrystal size measurements from the researchers were 9.7 ± 2.1 nm with a size distribution of 22% ($N = 311$) and 12.6 ± 4.4 nm with a size distribution of 35% ($N = 310$), respectively. For the LARP method, the average size measurements were 10.6 ± 2.2 nm with a size distribution of 21% ($N = 300$) and 11.9 ± 4.4 nm with a size distribution of 37% ($N = 310$). The manually measured average sizes were comparable to those outputted by the pipeline, as all were within a single standard deviation of each other (Table 2). However, the manual measurements varied significantly when it came to the size distributions. This is due in part to the inconsistency of manual measuring, which is exacerbated by the small population statistics (~300 each). This problem is eliminated when using the pipeline. Our pipeline completed both analyses within 10 min, with analysis of the nanocrystals from the LARP method ($N = 6{,}427$ nanocrystals) only taking about 3 min. The manual measurements took an average of 29 min to analyze the images of the hot-injection products and 33 min to analyze the images of the LARP products. The manual analyses yielded an average analysis throughput of *ca.* 10 nanocrystals/min, compared to the pipeline throughput of 6,270 nanocrystals/min. This signifies over a 600-fold increase in measurement efficiency using the pipeline.

The two datasets were then inputted into the previously published Autodetect-mNP pipeline to directly compare the accuracy and sensitivity of the two pipelines.[30] In comparison to the thousands of nanocrystals and several shape groups detected in our pipeline, only a few hundred nanocrystals from each dataset made it through the selection process in the Autodetect-mNP pipeline for analysis. The nanocrystals from both synthesis methods were also only grouped into two shape groups: one group that resembled cuboids and one group that resembled platelets, with nanocrystal edges that were rather jagged (Table 2 and Fig. S34† and S35†). In addition to losing analytical details through an oversimplification of morphology, quantitative information about each shape group was not accessible, nor realizable in 3D space. This demonstrates that not only is our pipeline capable of morphological differentiation of the same $CsPbBr_3$ nanocrystals prepared using two different synthesis methods, but it is also more accurate, precise, and efficient than current shape classification algorithms in the literature. While training a neural network is computationally-taxing, the evaluation of a trained neural network is efficient, so we expect this pipeline to be faster than other methods.

Table 2 Efficiency comparison of analysis methods.

	Automated Pipelines				***By-Hand***			
	Ref.[28]		***This Work***		***Researcher 1***		***Researcher 2***	
Synthesis method	***Hot injection***	***LARP***	***Hot injection***	***LARP***	***Hot injection***	***LARP***	***Hot injection***	***LARP***
Shape groups	2	2	4	6	—	—	—	—
Average size[a] (nm)	—	—	12.4	12.5	12.6	11.9	9.7	10.6
Size distribution ($\sigma/\bar{d}$)	—	—	0.33	0.50	0.35	0.37	0.22	0.21
Nanocrystal count (N)	331	489	7,082	6,427	310	310	311	300
Run time[b] (min:sec)	16:38	7:37	8:39	5:05	35:14	42:18	23:15	24:39

[a] Average major axis length across all shape groups.
[b] All code is run on a 32 GB 6-core Intel® i7 @ 2.6 GHz. All code (including ref.[28]) was run in its native OS environment.

Applicability to morphologically diverse ensembles. Fifty-two TEM images of colloidal nickel sulfide nanocrystals encompassing the complex phase space of that binary system (*e.g.*, Ni_3S_4, NiS, Ni_9S_8, and Ni_3S_2) were simultaneously inputted into the pipeline because of the morphological diversity amongst the various products (N = 13,132 nanocrystals). This allowed the pipeline to be tested across both phase and morphology for a large number of nanocrystals. The output yielded 10 statistically significant shape groups with *ccc* = 0.9369 (Fig. 6 and Fig. S36-S38†). Notably, each distinct phase of nickel sulfide, as assessed by powder X-ray diffraction, consisted of a unique combination of shape groups, illustrating the ability of the pipeline to differentiate between crystal phases with distinct nanocrystal morphologies. Phase-pure Ni_3S_2 nanocrystals were assigned to shape groups 7-10 with a primary contribution from groups 9 and 10 (Fig. 6a), demonstrating accurate identification of irregular, concave shapes, which as previously mentioned, has been an ongoing problem in shape classification in pipelines that can handle nanocrystal overlap.[19,29,30,35,45] Ni_3S_4 nanocrystals were assigned to shape groups 3-8 (Fig. 6b) and nicely display the classification of several shape groups in a single phase-pure sample. Ensembles of colloidal Ni_9S_8 nanocrystals were assigned to shape groups 1-8 (Fig. 6c), demonstrating an assessment of temporal reaction trajectories from quasi-spherical nanocrystals at early reaction times, to elongated rod-like structures at longer reaction times. NiS nanocrystals were assigned to shape groups 1-7 (Fig. 6d), showing successful classification of nanocrystals imaged at different magnifications. A classification algorithm trained with the data had an

accuracy of 99.5% (Fig. S14†). Additionally, the simultaneous classification of a large number of shape groups has not yet been demonstrated in the literature, and is particularly more difficult when done in an unsupervised nature due to the high level of precision in nanocrystal detection and analysis that is necessary for unassisted classification.[11,16,30]

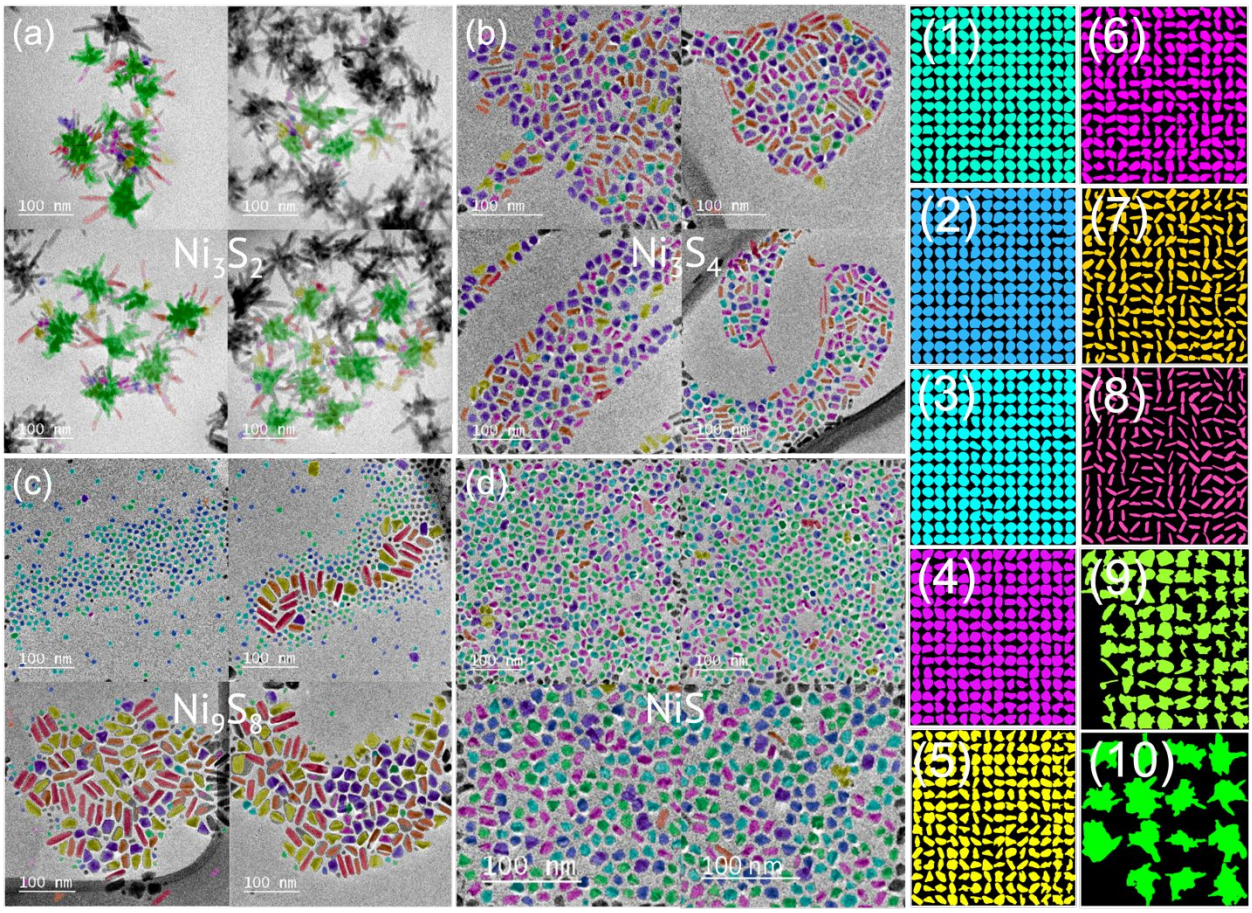

Fig. 6 Classification of a variety of nickel sulfide nanocrystals, illustrating the pipeline's ability to detect and quantify more morphologically diverse samples. Nanocrystals connected to edges have been removed. (a) Irregular, concave morphologies of Ni_3S_2. (b) Morphological diversity observed in phase pure Ni_3S_4. (c) Temporal reaction trajectory of morphology changes in Ni_9S_8. (d) Magnification differences in TEM images of NiS. (1-10) Colored segregation of $\leq$ 210 representative nickel sulfide nanocrystals into the 10 distinct shape groups.

Conclusions

We successfully created an unbiased ground truth for nanocrystal morphology analysis by stochastically simulating individual 2D nanocrystal TEM images from a 3D parameter space to train a convolutional neural network. We then used improved computer vision techniques and the trained network to predict the morphological parameters for each experimental image. This labeled data offers a significant improvement in accuracy for both unsupervised clustering and the training of a morphology classification algorithm. We demonstrated this by coding a fully automated pipeline to identify, label, and classify nanocrystals from experimental TEM images. The neural

network portion of the pipeline outputs each nanocrystal image labeled with a quantitative morphology definition comprised of three parameters from the CNN and the values of 30 morphology features. Once shape groups have been assigned *via* unsupervised clustering and appended to the dataset, the pipeline outputs the average value and standard deviation of all 30 features for each distinct group, histograms and their corresponding normal distributions for each predictor variable across each group, a linkage tree dendrogram of the population, a parallel coordinate plot, a Pareto chart of the principal components, a 3D scatter plot of the parameter space with groups indicated by color, visualizations of the groupings overlaid onto the original TEM images, exemplary nanocrystal morphologies of each group in a montage, a montage of the total classified nanocrystals to show relative population sizes of each group, the average size and standard deviation of the input nanocrystal ensemble as a whole, and the confusion matrix and classification accuracy from the classification algorithm training.

This simple, time-efficient pipeline will facilitate more accurate mapping between nanocrystal morphology and applications in synthetic optimizations, mechanistic studies involving size and shape, and morphology-function relationships. We demonstrate this by successfully quantifying morphological reproducibility, differentiating morphological characteristics between $CsPbBr_3$ nanocrystals prepared using two different synthetic methods, and quantifying several different morphologically diverse crystal phases of binary nickel sulfide nanocrystals. Not only is the pipeline sensitive enough to identify nuances in nanocrystal populations that are limited when using manual assessments, but these studies explicitly demonstrate improved generalizability over current morphology classification algorithms found in the literature. This offers a route to accurately automate and normalize TEM analysis for a wide range of nanocrystal sizes and shapes across images of differing quality, contrast, magnification, and resolution, while concurrently demonstrating more than a 600-fold improvement in efficiency over the currently accepted by-hand measurement.

Looking forward, there is room for improvement *via* 3D reconstruction using tilt-series of TEM images to validate the method. However, the generalizability and high-throughput nature of the pipeline could enable widespread implementation of the output shape parameters as quantitative definitions of individual 2D morphologies, affording standardization of nanocrystal morphology reporting across the literature. This would facilitate cohesion of experimental findings and consequentially aid in the implementation of data-driven learning (*via* the compilation of large datasets). Additionally, the continuous, yet low dimensional nature of nanocrystal morphologies described as CNN triplets creates a theoretically infinite, yet mappable morphological parameter space in 3D (*i.e.*, visualizable), as compared to the high dimensionality needed to utilize continuous physical features. Targeted points can therefore be readily determined and utilized for optimizing syntheses based on morphology using simple tools like regression, which is something that the discrete nature of qualitative labels make extremely complex and impractical. Such applications pave a pathway towards further investigations of morphology-dependent process-structure-property relationships using this pipeline, which we are currently working on with different materials.

Author contributions

‡These authors contributed equally.

Conflicts of interest

There are no conflicts to declare.

Acknowledgements

The synthetic nanocrystal chemistry was supported by the U.S. Department of Energy, Office of Science, Basic Energy Sciences, under Award DE-FG02-11ER46826. The ML pipeline development was supported by a SEED Award from Research Corporation for Science Advancement to R.L.B.

Footnotes

* Corresponding author

[a] Department of Chemistry, University of Southern California, Los Angeles, CA 90089, United States

E-mail: brutchey@usc.edu

† Electronic supplementary information (ESI) available. Additional information on the experimental methods and the methods used to create the pipeline, including methodological explanations, equations, and evaluations; comprehensive visualizations of the pipeline output and further analysis of the data used in the study. See DOI:

The code used in the pipeline as well as a how-to guide for implementation is available at: https://github.com/EmilyWill330/TEMPipeline.git

References

1 X. Peng, L. Manna, W. Yang, J. Wickham, E. Scher, A. Kadavanich and A. P. Alivisatos, *Nature*, 2000, **404**, 59–61.
2 S. Link and M. A. El-Sayed, *Int. Rev. Phys. Chem.*, 2000, **19**, 409–453.
3 M. Kruszynska, H. Borchert, A. Bachmatiuk, M. H. Rümmeli, B. Büchner, J. Parisi and J. Kolny-Olesiak, *ACS Nano*, 2012, **6**, 5889–5896.
4 A. Leonardi and M. Engel, *ACS Nano*, 2018, **12**, 9186–9195.
5 J. Billet, W. Dujardin, K. De Keukeleere, K. De Buysser, J. De Roo and I. Van Driessche, *Chem. Mater.*, 2018, **30**, 4298–4306.
6 Q. Liu, A. Díaz, A. Prosvirin, Z. Luo and J. D. Batteas, *Nanoscale*, 2014, **6**, 8935–8942.
7 Y. Fu, H. Zhu, J. Chen, M. P. Hautzinger, X.-Y. Zhu and S. Jin, *Nat. Rev. Mater.*, 2019, **4**, 169–188.
8 R. Narayanan and M. A. El-Sayed, *Nano Lett.*, 2004, **4**, 1343–1348.
9 M. Subhramannia and V. K. Pillai, *J. Mater. Chem.*, 2008, **18**, 5858.
10 J. Shi, K. Lei, W. Sun, F. Li, F. Cheng and J. Chen, *Nano Res.*, 2017, **10**, 3836–3847.
11 L. Boselli, H. Lopez, W. Zhang, Q. Cai, V. A. Giannone, J. Li, A. Moura, J. M. de Araujo, J. Cookman, V. Castagnola, Y. Yan and K. A. Dawson, *Commun. Mater.*, 2020, **1**, 35.
12 C. J. Murphy and J. M. Buriak, *Chem. Mater.*, 2015, **27**, 4911–4913.

13 W. D. Pyrz and D. J. Buttrey, *Langmuir*, 2008, **24**, 11350–11360.
14 A. Kreshuk, U. Koethe, E. Pax, D. D. Bock and F. A. Hamprecht, *PLoS ONE*, 2014, **9**, e87351.
15 J. M. Sosa, D. E. Huber, B. Welk and H. L. Fraser, *Integrating Mater. Manuf. Innov.*, 2014, **3**, 123–140.
16 H. Wen, X. Xu, S. Cheong, S.-C. Lo, J.-H. Chen, S. L. Y. Chang and C. Dwyer, *Nanoscale Adv.*, 2021, **3**, 6956–6964.
17 M. Schorb, I. Haberbosch, W. J. H. Hagen, Y. Schwab and D. N. Mastronarde, *Nat. Methods*, 2019, **16**, 471–477.
18 Y. Qian, J. Z. Huang, X. Li and Y. Ding, *IEEE Trans. Image Process.*, 2016, **25**, 5713–5726.
19 Chiwoo Park, J. Z. Huang, J. X. Ji, and Yu Ding, *IEEE Trans. Pattern Anal. Mach. Intell.*, 2013, **35**, 1–1.
20 L. Cervera Gontard, D. Ozkaya and R. E. Dunin-Borkowski, *Ultramicroscopy*, 2011, **111**, 101–106.
21 B. Lee, S. Yoon, J. W. Lee, Y. Kim, J. Chang, J. Yun, J. C. Ro, J.-S. Lee and J. H. Lee, *ACS Nano*, 2020, **14**, 17125–17133.
22 X. Hu, F. Li, F. Xia, X. Guo, N. Wang, L. Liang, B. Yang, K. Fan, X. Yan and D. Ling, *J. Am. Chem. Soc.*, 2020, **142**, 1636–1644.
23 B. Lim, P. H. C. Camargo and Y. Xia, *Langmuir*, 2008, **24**, 10437–10442.
24 G. Barim, S. R. Smock, P. D. Antunez, D. Glaser and R. L. Brutchey, *Nanoscale*, 2018, **10**, 16298–16306.
25 M. Calvaresi, *Nat. Nanotechnol.*, 2020, **15**, 512–513.
26 K. A. Brown, S. Brittman, N. Maccaferri, D. Jariwala and U. Celano, *Nano Lett.*, 2020, **20**, 2-10.
27 S. Sacanna, D. J. Pine and G.-R. Yi, *Soft Matter*, 2013, **9**, 8096.
28 E. Kim, K. Huang, A. Saunders, A. McCallum, G. Ceder and E. Olivetti, *Chem. Mater.*, 2017, **29**, 9436–9444.
29 C. R. Laramy, K. A. Brown, M. N. O'Brien and Chad. A. Mirkin, *ACS Nano*, 2015, **9**, 12488–12495.
30 X. Wang, J. Li, H. D. Ha, J. C. Dahl, J. C. Ondry, I. Moreno-Hernandez, T. Head-Gordon and A. P. Alivisatos, *JACS Au*, 2021, **1**, 316–327.
31 L. Bezinge, R. M. Maceiczyk, I. Lignos, M. V. Kovalenko and A. J. DeMello, *ACS Appl Mater Interfaces*, 2018, **10**, 18869-18878.
32 O. Wetzel, O. Prymak, K. Loza, N. Gumbiowski, M. Heggen, P. Bayer, C. Beuck, C. Weidenthaler and M. Epple, *Inorg. Chem.*, 2022, **Article ASAP**, DOI: 10.1021/acs.inorgchem.2c00281.
33 H. Tao, T. Wu, M. Aldeghi, T. C. Wu, A. Aspuru-Guzik and E. Kumacheva, *Nat. Rev. Mater.*, 2021, **6**, 701-716.
34 E. J. Braham, R. D. Davidson, M. Al-Hashimi, R. Arróyave and S. Banerjee, *Dalton Trans.*, 2020, **49**, 11480-11488.
35 H. Kim, J. Han and T. Y.-J. Han, *Nanoscale*, 2020, **12**, 19461-19469.
36 C. Park and Y. Ding, *MRS Commun.*, 2019, **9**, 545–555.
37 L. Mill, D. Wolff, N. Gerrits, P. Philipp, L. Kling, F. Vollnhals, A. Ignatenko, C. Jaremenko, Y. Huang, O. De Castro, J. Audinot, I. Nelissen, T. Wirtz, A. Maier and S. Christiansen, *Small Methods*, 2021, 2100223.

38 C. K. Groschner, C. Choi and M. C. Scott, *Microsc. Microanal.*, 2021, **27**, 549–556.
39 H. Wen, J. M. Luna-Romera, J. C. Riquelme, C. Dwyer and S. L. Y. Chang, *Nanomaterials*, 2021, **11**, 2706.
40 S. R. Spurgeon, C. Ophus, L. Jones, A. Petford-Long, S. V. Kalinin, M. J. Olszta, R. E. Dunin-Borkowski, N. Salmon, K. Hattar, W.-C. D. Yang, R. Sharma, Y. Du, A. Chiaramonti, H. Zheng, E. C. Buck, L. Kovarik, R. L. Penn, D. Li, X. Zhang, M. Murayama and M. L. Taheri, *Nat. Mater.*, 2021, **20**, 274–279.
41 L. Yao, Z. Ou, B. Luo, C. Xu and Q. Chen, *ACS Cent. Sci.*, 2020, **6**, 1421–1430.
42 N. O'Mahony, S. Campbell, A. Carvalho, S. Harapanahalli, G. V. Hernandez, L. Krpalkova, D. Riordan and J. Walsh, in *Advances in Computer Vision*, eds. K. Arai and S. Kapoor, Springer International Publishing, Cham, 2020, vol. 943, pp. 128–144.
43 N. Artrith, K. T. Butler, F.-X. Coudert, S. Han, O. Isayev, A. Jain and A. Walsh, *Nat. Chem.*, 2021, **13**, 505–508.
44 B. Lin, N. Emami, D. A. Santos, Y. Luo, S. Banerjee and B.-X. Xu, *Npj Comput. Mater.*, 2022, **8**, 88.
45 C. Park, J. Z. Huang, D. Huitink, S. Kundu, B. K. Mallick, H. Liang and Y. Ding, *IIE Trans.*, 2012, **44**, 507–522.
46 L. Fox, *Math. Gaz.*, 1969, **53**, 222–224.
47 S. Shalev-Shwartz and S. Ben-David, *Understanding machine learning: from theory to algorithms*, Cambridge University Press, New York, NY, USA, 2014.
48 *MathWorks Statistics and Machine Learning Toolbox: Documentation*, MathWorks, 2022.
49 G. Yamankurt, E. J. Berns, A. Xue, A. Lee, N. Bagheri, M. Mrksich and C. A. Mirkin, *Nat. Biomed. Eng.*, 2019, **3**, 318–327.
50 S. Wei, Y. Yang, X. Kang, L. Wang, L. Huang and D. Pan, *Chem. Commun.*, 2016, **52**, 7265–7268.
51 L. Protesescu, S. Yakunin, M. I. Bodnarchuk, F. Krieg, R. Caputo, C. H. Hendon, R. X. Yang, A. Walsh and M. V. Kovalenko, *Nano Lett.*, 2015, **15**, 3692–3696.
52 D. Dresen, A. Qdemat, S. Ulusoy, F. Mees, D. Zákutná, E. Wetterskog, E. Kentzinger, G. Salazar-Alvarez and S. Disch, *J. Phys. Chem. C*, 2021, **125**, 23356–23363.
53 C. B. Murray, D. J. Norris and M. G. Bawendi, *J. Am. Chem. Soc.*, 1993, **115**, 8706–8715.